https://doi.org/10.32604/zkg.2026.079534

ARTICLE

Research on the modification of high-temperature resistance performance of magnesium potassium phosphate cement by compound admixtures

Yutong Zhou[1], Zheng Zhou[1,*], Lvchao Qiu[1], Zhoufeng Zhao[1], Kuangda Lu[1], Liting Wang[2], Bo Peng[2], Shouwei Jian[2] and Hongbo Tan[2]
[1]State Grid Zhejiang Electric Power Research Institute, Hangzhou, China
[2]State Key Laboratory of Silicate Materials for Architectures, Wuhan University of Technology, Wuhan, China
*Corresponding Author: Zheng Zhou. Email: zhengzifd@126.com

Received: 22 January 2026; Accepted: 25 March 2026

ABSTRACT: Magnesium potassium phosphate cement (MKPC) exhibits strength degradation and volume shrinkage under high-temperature conditions, which hinders its application in high-temperature scenarios. The effects of aluminium hydroxide (AH) and basalt fiber (BF) on the room-temperature properties and high-temperature resistance of MKPC were investigated using XRD, SEM, and EDS. The strength results showed that incorporating 15% aluminium hydroxide increases the residual strength of MKPC by 48.87% to 101.59% following heat treatment at 200~1100°C. The presence of basalt fibers reduced the volumetric changes of MKPC after heat treatment, but led to a decrease in the residual strength. The microstructural test results showed that aluminium hydroxide markedly promoted the formation of refractory phases, including α-active alumina and magnesium aluminate spinel, at high temperatures, whereas debonding was observed in specimens incorporating basalt fibers. Based on the above experimental results, the coupled effects of aluminium hydroxide and basalt fibers on the high-temperature resistance of MKPC were discussed. The research findings may provide insights for the application of MKPC in high-temperature scenarios.

KEYWORDS: Magnesium phosphate; aluminium hydroxide; basalt fiber; high-temperature resistance

1 Introduction

Magnesium potassium phosphate cement (MKPC) is a rapid-setting cementitious material composed of dead-burned magnesium oxide, soluble phosphate, retarder, water, and other admixtures mixed at specific proportions [1]. Owing to its rapid setting and hardening, high early strength, and excellent bonding performance [2, 3], MKPC has been widely investigated for applications such as rapid repair materials, building restoration [4, 5], and hazardous waste stabilization [6]. The main hydration reaction of MKPC is shown in Equation (1). Compared with ordinary Portland cement [7], the struvite-dominated hydration products of MKPC exhibit relatively high thermal stability [8, 9], which makes MKPC a promising binder for high-temperature applications [10, 11]. Although the fire resistance of MKPC is superior to that of traditional cementitious materials, it still tends to experience strength degradation and volume shrinkage due to the removal of bound water under high temperatures, resulting in cracking and peeling [12]. Therefore, considerable efforts have been devoted to investigating the high-temperature stability of MKPC. Incorporating refractory fillers into MKPC has been the most prevalent approach to enhancing its high-temperature performance.

$$MgO + PO_4(s) + 5H_2O \rightarrow MgKPO_4 \cdot 6H_2O \text{ (struvite)} \quad (1)$$

Over the past decade, incorporating refractory fillers into MKPC has been the most prevalent approach to enhancing its high-temperature performance. Li et al. [13] demonstrated that incorporating appropriate quantities of hollow glass microspheres enhances MKPC strength and fire resistance while reducing its density and thermal conductivity. Low-density fillers such as expanded perlite and expanded vermiculite also effectively mitigate strength degradation in MKPC at high temperatures and reduce crack formation caused by thermal stress [14, 15]. Furthermore, mineral admixtures such as fly ash and silica fume promote the formation of refractory phases and the sintering of non-crystalline grains within MKPC under high-temperature conditions [16, 17]. This results in the development of a ceramic-like

MATERIALS

structure, thereby enhancing the residual strength of MKPC after high-temperature exposure [18]. Although the incorporation of lightweight refractory fillers and mineral additives can mitigate the strength degradation of MKPC at high temperatures, it may also result in insufficient strength at room temperature and reduced volumetric stability.

To further mitigate high-temperature degradation and enhance structural stability, some studies have incorporated reinforcing fibres and flame-retardant compounds into fire-resistant materials [19]. Such functional components can improve high-temperature resistance through crack bridging and thermal buffering effects, thereby reducing heat-induced damage and strength loss. For instance, Yasir et al. [20, 21] noted that basalt fibres suppress crack propagation and maintain load transfer at high temperatures, thus enhancing thermal stability and mechanical properties. Lou et al. [22] confirmed that incorporating aluminium hydroxide modulates heat absorption behaviour and microstructural integrity during thermal exposure, thereby enhancing high-temperature stability. Consequently, further incorporating fibres and flame retardants into MKPC holds promise for simultaneously addressing strength retention and high-temperature stability [23]. However, current research on the high-temperature modification of aluminium hydroxide (AH) and basalt fibre (BF) has primarily focused on organic refractory materials, with limited studies investigating their application in MKPC [18]. To date, few studies have been reported on the impact of such modifications on the high-temperature resistance of MKPC.

This study investigates the effects of aluminium hydroxide and basalt fibres on the high-temperature behaviour of a lightweight MKPC composite containing expanded vermiculite and hollow glass microspheres. The setting time and room-temperature compressive strength of each mixture were tested, together with the residual strength, mass loss, and volume change of specimens after heat treatment at 200, 400, 600, 800, 1000, and 1100°C. The phase evolution and microstructural changes of representative specimens before and after heating were analysed by XRD, SEM, and EDS. In addition, the effects of AH and BF on the high-temperature resistance of this lightweight MKPC system were discussed. The findings are expected to provide a basis for the design of lightweight fire-resistant and thermal-insulating MKPC-based composites for non-load-bearing high-temperature applications.

2 Materials and methods

2.1 Raw materials

In this study, the raw materials for the test specimens were divided into binders, retarders, fillers, and admixtures. Dead-burned magnesium oxide (MgO) and potassium dihydrogen phosphate (KH_2PO_4) were used as binders, borax ($Na_2B_4O_7{\cdot}10H_2O$) served as the retarder, hollow glass microspheres and expanded vermiculite were used as fillers, and aluminium hydroxide (AH) and basalt fiber (BF) were added as admixtures. It is worth noting that potassium dihydrogen phosphate, borax, and aluminium hydroxide were all industrial-grade materials with purities ranging from 95% to 97%, and particle sizes below 70 µm. The diameter of basalt fibre is 25 µm, with a cut length of 3–5 mm. The chemical compositions of calcined magnesium oxide, hollow glass microspheres, expanded vermiculite, and basalt fibre are presented in Table 1. The XRD patterns of calcined magnesium oxide, hollow glass microspheres (HGM), and expanded vermiculite (EV) are presented in Figure 1.

2.2 Samples preparation

The mix design for MKPC composite materials is shown in Table 2. All mixtures employ identical quantities of binder, retarder, filler, and water. The binder for each mixture comprises magnesium oxide and potassium dihydrogen phosphate in a molar ratio of 3:1, the retarder is incorporated at 5% by mass of the binder, and water is added at 50% of the combined mass of binder and filler. The fillers in each mixture comprised equal quantities of EV and HGM, both added at 20% of the binder mass. These dosages were selected based on previous studies on lightweight/refractory filler modification of MKPC [21, 24–27], together with our preliminary experimental screening, in which this dosage range provided a relatively stable lightweight refractory skeleton while maintaining acceptable workability and measurable residual strength after heat treatment. Within the mixtures, groups AH5 to AH20 investigated the effect of aluminium hydroxide, with its content set between 5% and 20% of the binder mass. Groups BF0.5 to BF2.0 investigated the effect of basalt fibre, with its content set at 0.5% to 2% of the binder mass. Other Groups examined

Table 1 The chemical composition of raw materials (wt.%)

Binder	MgO	SiO_2	CaO	Fe_2O_3	Al_2O_3	K_2O	Na_2O	LOI
MgO	89.517	3.309	1.933	1.684	0.893	0.037	/	1.808
HGM	/	82.353	8.237	0.136	0.123	0.006	1.381	6.944
EV	10.366	44.079	2.358	13.624	15.846	5.238	/	4.057
BF	9.358	50.196	6.977	10.232	16.734	1.258	1.092	3.048

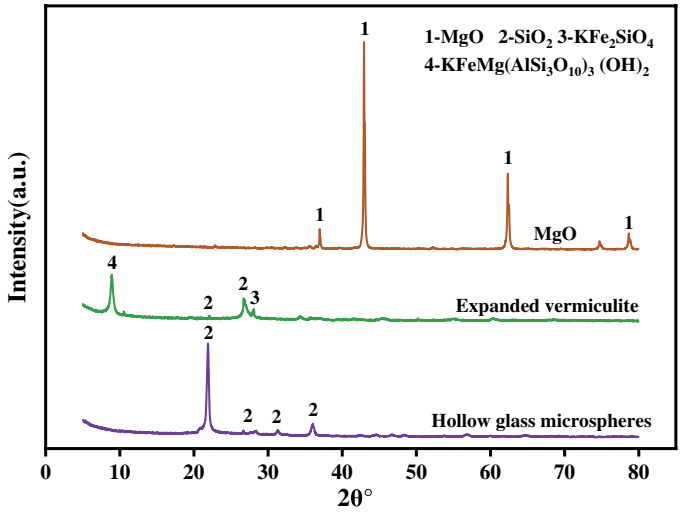

Figure 1 XRD patterns of raw materials: MgO, expanded vermiculite (EV) and hollow glass microspheres (HGM)

Table 2 The mix proportions of the MKPC composites

Number	Mixtures	Binder	Retarder	Fillers		Admixture		Water
		M:P	Borax(%)	EV (%)	HGM (%)	AH (%)	BF (%)	W/(MPC + Fillers)
0	Blank	3:1	5	20	20	/	/	0.5
1	AH5	3:1	5	20	20	5	/	0.5
2	AH10	3:1	5	20	20	10	/	0.5
3	AH15	3:1	5	20	20	15	/	0.5
4	AH20	3:1	5	20	20	20	/	0.5
5	BF0.5	3:1	5	20	20	/	0.5	0.5
6	BF1.0	3:1	5	20	20	/	1.0	0.5
7	BF1.5	3:1	5	20	20	/	1.5	0.5
8	BF2.0	3:1	5	20	20	/	2.0	0.5
9	AH5-BF2.0	3:1	5	20	20	5	2.0	0.5
10	AH20-BF0.5	3:1	5	20	20	20	0.5	0.5
11	AH15-BF1.0	3:1	5	20	20	15	1.0	0.5
12	AH10-BF1.5	3:1	5	20	20	10	1.5	0.5
13	AH20-BF2.0	3:1	5	20	20	20	2.0	0.5
14	AH5-BF0.5	3:1	5	20	20	5	0.5	0.5

the combined effect of aluminium hydroxide and basalt fibre.

The specimens were prepared with reference to GB/T 17671-2021. First, all powdered raw materials were weighed according to the proportions listed in Table 2 and dry-mixed to ensure uniform distribution. Water was then added, and the mixture was mechanically stirred until a homogeneous slurry was obtained. Then, the slurry was poured into standard moulds measuring 40 mm × 40 mm × 40 mm. Upon completion of pouring, cling film was applied to minimise moisture evaporation. Once the specimens had undergone initial setting, demoulding was performed. After demoulding, the specimens were transferred to a standard curing chamber maintained at 20 ± 2°C and 60 ± 5% relative humidity, where they underwent constant temperature and humidity curing for 7 d. Finally, specimens cured to the corresponding age were placed in a forced-air drying oven at 40°C until mass stability was achieved. They were then removed for subsequent macroscopic performance testing and microscopic characterisation. Furthermore, to ensure the reliability and reproducibility of experimental data, all macroscopic performance indicators were tested using at least three parallel specimens, with the test results being the average value of these specimens.

2.3 Testing procedure

The testing of each mixture in this paper may be divided into macroscopic and microscopic performance aspects. Regarding macroscopic performance, the setting time at room temperature, compressive strength at 7 d, and changes in strength, mass, and volume before and after heat treatment at various temperatures were assessed for each mixture. Regarding microstructural

performance, XRD patterns and SEM images of the hydrated samples were examined before and after heat treatment. Elemental analysis of the sample surfaces was conducted using EDS point-scanning techniques. Detailed testing methodologies and references are provided in Sections 2.3.1 and 2.3.2.

2.3.1 Macroscopic performance

All tests for setting time of mixtures were conducted in accordance with GB/T 1346-2024. During testing, freshly mixed slurry was poured into setting time test moulds, levelled using a trowel, and then subjected to setting time measurement via a vicat apparatus. Compressive strength testing for all mixtures followed GB/T 17671-2021 standards, employing a universal testing machine with a loading rate of 0.2 kN/s.

To evaluate the high-temperature behaviour of each mixture group, all specimens cured to the specified age were dried to constant weight before undergoing heat treatment at temperatures of 200°C, 400°C, 600°C, 800°C, 1000°C, and 1100°C. The heat treatment process was conducted in a high-temperature sintering furnace and comprised three stages: Firstly involved heating from an initial temperature of 20°C to the target temperature at a heating rate of 10°C/min. Secondly, holding at the target temperature for 2 h. Finally, the thermal treatment was concluded, with samples cooling naturally within the furnace to room temperature. The initial mass (m_0) of the sample prior to heat treatment and the mass (m_1) after heat treatment were measured using a high-precision electronic balance, from which the mass loss rate was calculated. The dimensions of the sample before and after heat treatment were measured using a vernier caliper, enabling the calculation of the initial volume (V_0) of the sample before heat treatment and the volume (V_1) after heat treatment, thereby determining the volume shrinkage rate. The specific calculation method is as follows:

$$S = \left(\frac{m_0 - m_1}{m_0}\right) \times 100\% \quad (2)$$

$$\pi = \mathrm{F}\left(\frac{V_0 - V_1}{V_0}\right) \times 100\% \quad (3)$$

2.3.2 Microscopic characterisation

After the compressive strength test, several thin fragments were selected from the fracture surface. A portion of these fragments was used for SEM imaging and EDS point-scanning elemental distribution analysis, while the remainder was ground and sieved through a 200~mesh screen for XRD pattern testing. The XRD patterns were analysed using an X-ray diffractometer manufactured by Empyrean of the Netherlands. The scanning speed during testing was 10°/min, with a step size of 0.02° and a measurement range from 5° to 80°. The SEM images were obtained by a Quanta FEG 450 scanning electron microscope manufactured in the United States. The testing process was conducted at an operating voltage of 15 kV, with magnification ranging from 1000 to 3000 times. The samples underwent sputter-coated platinum treatment prior to testing.

3 Results and discussion

3.1 Setting time

Figure 2 illustrates the effects of aluminium hydroxide (AH), basalt fibre (BF), and their combined action on the initial setting time and final setting time of MKPC. The control group exhibited an initial setting time of 189 min and a final setting time of 259 min, with a setting interval of 70 min. This indicates a protracted transitional phase between the loss of plasticity and complete hardening of the slurry.

As shown in Figure 2a, both the initial and final setting times of the mixture decreased monotonically as the AH content increased from 5% to 20%. At an AH content of 20%, the initial setting time was reduced to 101 min, whilst the final setting time decreased to 131 min. Compared to the control group, the AH20 group exhibited a 46.56% reduction in initial setting time and a 49.42% reduction in final setting time. This effect may be attributed to the dual action of AH in fresh MKPC slurry: firstly, the minute AH particles increase the bulk density of solids and provide additional heterogeneous nucleation surfaces, thereby promoting the early formation of permeating hydration products. Secondly, the microfilling effect reduces the free water content within the slurry, accelerating the hydration process during the early age stages. Consequently, within the studied dosage range, both the initial setting time and the final setting time are shortened [28].

As shown in Figure 2b, both the initial setting time and final setting time exhibit a trend of initially decreasing followed by a gradual increase with rising BF content. At low BF dosages, BF significantly accelerated the setting process: the BF 0.5 mixture exhibited an initial setting time of 103 min and a final setting time of 137 min, representing reductions of 45.50% and 47.10% respectively, compared to the control group, with the setting interval shortened to 34 min. However, further increasing BF content led to delayed setting. The BF 2.0 mixture exhibited an initial setting time of 164 min and a final setting time of 228 min, with the setting interval extending to 64 min, which was close to that of the control group. This dual response of acceleration and delay can be attributed to competitive effects induced by fibre addition. At low BF dosages,

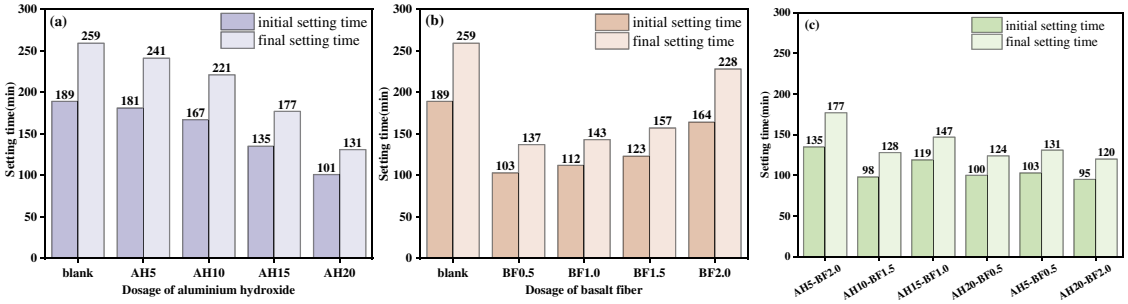

Figure 2 Initial and final setting times of MKPC composites under (a) AH mono-modification, (b) BF mono-modification, and (c) AH-BF co-modification

well-dispersed fibres provide interfacial sites that promote early precipitation and crystal growth of potassium magnesium phosphate hydrate, thereby accelerating rigidity development. Conversely, at high dosages, fibre agglomeration and the accompanying increase in rheological resistance impede ion transport, reduce reaction uniformity within the sample, and delay the formation of a continuous hardening network, consequently prolonging the final setting time [29].

As shown in Figure 2c, all mixtures modified with both AH and BF exhibited significantly shorter initial and final setting times compared to the control group and single-component modified groups. Among these, the AH20-BF2.0 and AH10-BF1.5 mixtures demonstrated the fastest setting rates, with initial setting times ranging from 90 to 100 min. The final setting time was 120–130 min, representing a reduction of nearly 50%, with a setting interval of only 25 min. The AH20-BF0.5 and AH10-BF1.5 groups exhibited similar trends. Overall, combined modification effectively accelerates the early setting process. However, from a practical construction perspective, the significantly reduced setting interval also implies a markedly shorter operational time window. This must be fully considered during sample preparation and handling procedures.

3.2 Compressive strength

Figure 3a–c illustrates the effects of aluminium hydroxide (AH), basalt fibre (BF), and their synergistic interaction on the compressive strength of MKPC at room temperature and its residual compressive strength after heat treatment. The figures reveal that within the 200~800°C range, the compressive strength of the control group progressively decreased with increasing heat treatment temperature. However, within the 1000~1100°C range, the samples exhibited a marked recovery in compressive strength. This outcome aligns with prior research on MKPC modified with hollow glass microspheres and expanded vermiculite [25, 30, 31].

As shown in Figure 3a, the addition of AH significantly enhances both the room-temperature strength and the residual strength after high-temperature treatment of MKPC. Specifically, the room-temperature compressive strength of MKPC increased from 2.06 MPa in the control group to 2.99 MPa in the AH20 group with rising AH content. Similarly, the residual strength of MKPC after heat treatment exhibited a trend of initial increase and then decrease with increasing AH content. At an AH content of 15%, the specimen strength reached 4.63 MPa after 200°C treatment and 4.25 MPa after 1100°C treatment, remaining below the room-temperature strength only after 800°C treatment. Compared to the control group,

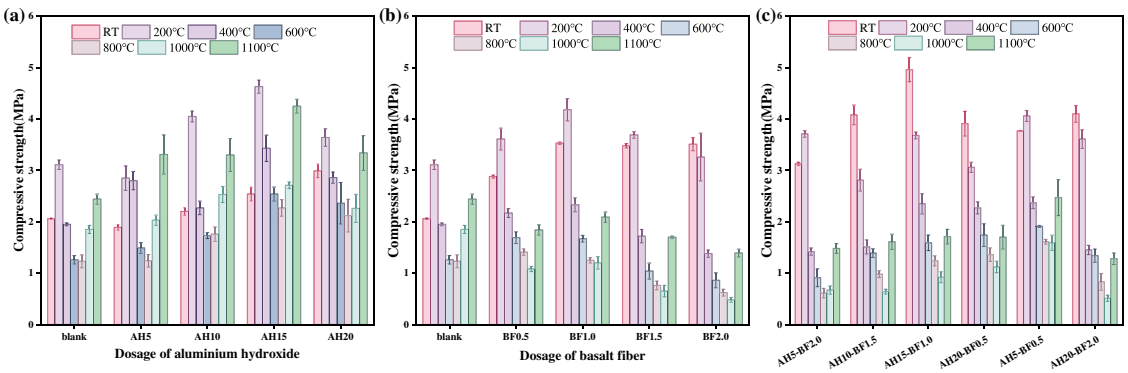

Figure 3 Compressive strength of MKPC composites at room temperature and residual strength after heat treatment: (a) AH-modified, (b) BF-modified, (c) AH-BF co-modified

the residual strength of the AH15 group increased by 48.87% to 101.59% following heat treatment at different temperatures. These results indicate that AH not only enhances the structural strength of MKPC hydration products but also improves the thermal stability of the MKPC structure.

As shown in Figure 3b, the incorporation of BF enhances the compressive strength of MKPC at room temperature. With increasing BF content, the room-temperature compressive strength exhibits a trend of initial improvement followed by plateauing. At a BF content of 1.5%, the compressive strength reaches a maximum value of 3.53 MPa (compared to 2.06 MPa for the control group). At a BF content of 2.0%, the strength was 3.50 MPa, remaining at a similar level. However, BF addition adversely affected the residual strength of MKPC after heat treatment. Specifically, following heat treatment at lower temperatures (≤200°C), the strength of BF-modified MKPC specimens continued to increase, exceeding that of the control group. Yet, from 400°C onwards, a marked deterioration in strength occurred. After treatment at 1000°C, BF 2.0 retained only 0.48 MPa, representing a mere 13.7% of its room-temperature strength. Notably, unlike the control group, the residual strength of BF-doped MKPC specimens after heat treatment did not begin to recover until 1100°C. This indicates that BF addition not only introduces thermosensitive structural defects, leading to reduced strength stability, but also influences the initial temperature at which the ceramicisation reaction occurs within the MKPC system.

As shown in Figure 3c, the room-temperature compressive strength of MKPC specimens co-modified with AH and BF was significantly enhanced, though their high-temperature performance remained susceptible to BF degradation effects. Specifically, under ambient conditions, all co-modified mixtures exhibit superior strength to the control group, with the AH15-BF1.0 formulation demonstrating the highest room-temperature strength at 4.96 MPa. Following treatment at 200°C, some mixtures retained relatively high residual strengths, with AH5-BF0.5 and AH15-BF1.0 demonstrating particularly outstanding performance. When the temperature rose to 400°C, residual strengths generally declined. Groups with low BF content exhibited relatively stable strength after heat treatment, whereas those with high BF content showed a more pronounced decrease. At 600~800°C, residual strength was approximately half that of the control group. When temperatures reached 1000~1100°C, only AH5-BF0.5 retained residual strength close to the control group, while groups with high BF content remained significantly weaker.

3.3 Mass loss

Figure 4a–c illustrates the effects of AH and BF on the mass loss rate of MKPC composites following heat treatment: the mass loss rate of the control group increased steadily with rising heat treatment temperatures, from 18.542% at 200°C to 25.868% at 1100°C. Notably, the incremental mass loss within the 1000~1100°C temperature range was significantly higher than that observed between 200~800°C. Previous studies attribute this disparity to decomposition and sintering reactions occurring in the expanded vermiculite and hollow glass microspheres fillers at high temperatures [32–34].

The effect of AH on mass loss of MKPC following heat treatment is rather complex, being jointly influenced by its content and heat treatment temperature. Specifically, within the AH5 to AH20 groups, at temperatures ranging from 200°C to 400°C, the mass loss rate of MKPC initially increases, then decreases with rising AH content. However, within the 600°C to 1100°C temperature range, this trend reversed: the mass loss in the AH5 and AH10 groups exceeded that of the control group, while the mass loss in the AH15 and AH20 groups was reduced. This occurs because, following AH incorporation, mass loss in the MKPC system stems from multiple sources: dehydration of struvite crystals, dehydration of aluminium hydroxide, decomposition of fillers, and ceramicisation. As the dehydration process of aluminium hydroxide absorbs a significant amount of heat, its high

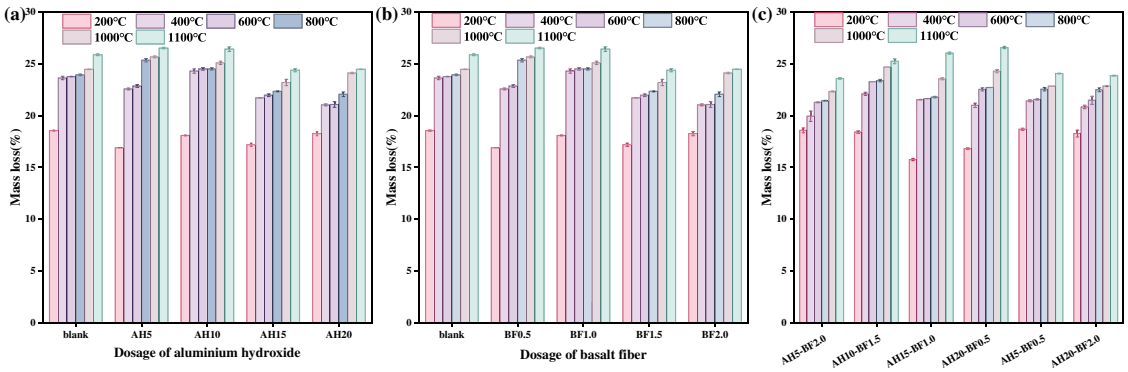

Figure 4 Mass loss of MKPC composites after heat treatment: (a) AH-modified, (b) BF-modified, (c) AH-BF co-modified

content can reduce mass loss caused by MKPC filler decomposition at high heat treatment temperatures. However, at lower temperatures, the dehydration of aluminium hydroxide itself increases mass loss [35–37].

In contrast, the influence of BF on the mass loss of MKPC after heat treatment exhibited a relatively clear temperature dependence. At 200~400°C, the BF0.5 group showed the lowest mass loss among the BF-modified groups, indicating that a low BF dosage was more effective in reducing mass loss at low temperatures. In comparison, at 800~1100°C, the mixtures containing 1.5–2.0 wt.% BF showed better mass retention. Combining X-ray fluorescence (XRF) analysis with prior research, this is attributed to the softening and decomposition of calcium-containing components within BF at 800°C. Additionally, when AH and BF jointly modify MKPC, the overall suppression of mass loss is greater than with either modifier alone, particularly within the low-temperature range of 200~400°C where this inhibitory effect is most pronounced. For instance, the AH15-BF1.0 group exhibited the lowest mass loss rate at 200°C among all experimental groups. At high temperatures, the co-modified groups with high BF and low AH ratios demonstrated the best performance in preserving MKPC mass. In summary, the combined modification of AH and BF demonstrated superior overall performance in controlling mass loss of MKPC following heat treatment compared to either AH or BF acting alone.

3.4 Volume shrinkage

Figure 5a–c illustrates the influence of AH and BF additives on the volumetric shrinkage of magnesium potassium phosphate cement (MKPC) following heat treatment at varying temperatures. It is evident that the control group exhibits a volumetric shrinkage rate, which initially increases gradually before rising sharply with increasing temperature, peaking at 1000°C. At 1100°C, it decreases slightly. This occurs because within the 200~600°C temperature range, MKPC hydration products undergo dehydration decomposition, generating numerous micro-pores within the matrix and causing an initial contraction. Subsequently, at temperatures between 800~1000°C, the interlayer structure of expanded vermiculite is disrupted, while hollow glass microspheres begin to soften, leading to a second contraction phase. Upon reaching 1100°C, the system exhibits slight sintering and densification. Certain phases undergo secondary reactions, producing minimal expansion that partially offsets the contraction, resulting in a slight decrease in the shrinkage rate [30, 38].

As shown in Figure 5a, AH effectively inhibits shrinkage under medium temperature conditions, but this inhibitory effect diminishes markedly as temperatures rise further. Within the 200~800°C temperature range, all mixtures containing AH exhibited lower shrinkage rates than the control group. Among these, AH15 demonstrated the most pronounced shrinkage inhibition, reducing volumetric shrinkage by 15% to 20% relative to the control. At temperatures of 1000~1100°C, although low AH content still inhibited MKPC's volumetric shrinkage, excessive AH addition caused the shrinkage rate of the AH20 group to exceed that of the blank control. This indicates that excessive aluminium hydroxide leads to diminished volumetric stability under extreme high temperatures. This phenomenon confirms aluminium hydroxide's dual role: at low temperatures, micro-filling and early densification limit thermally induced volume changes. At high temperatures, AH decomposition into α-Al_2O_3 potentially reinforces the matrix structure [35]. However, at extremely high temperatures, excessive AH addition exacerbates pore formation due to decomposition, disrupting matrix continuity and undermining the system's ability to maintain volumetric integrity.

As shown in Figure 5b, the volume shrinkage rate of the BF-modified mixture after heat treatment remained lower than that of the control group across the entire temperature range, with the inhibitory effect increasing with higher BF content. Specifically, within the 200~600°C range, the 2.0% BF mixture exhibited a reduction

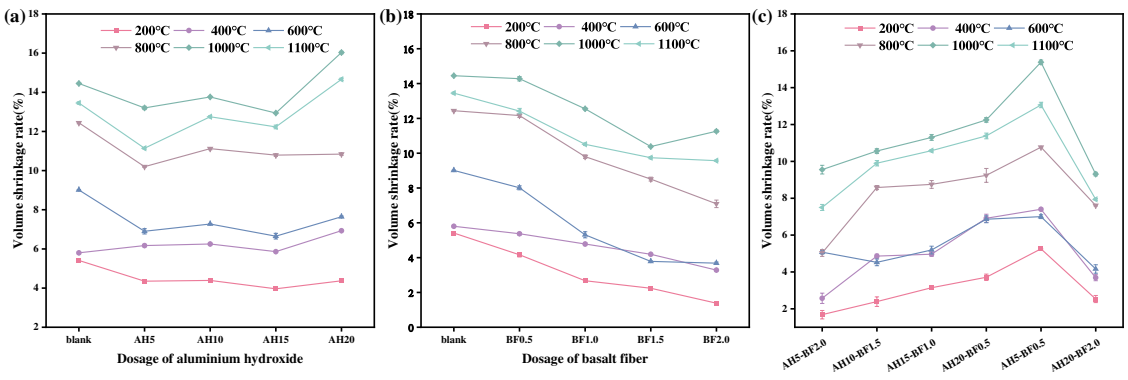

Figure 5 Volume shrinkage of MKPC composites after heat treatment: (a) AH-modified, (b) BF-modified, (c) AH-BF co-modified

in shrinkage of approximately 50~74% compared to the baseline value, significantly mitigating thermal shrinkage. This is primarily attributable to BF's excellent stability within this temperature range. BF effectively fills internal pores within MKPC, enhancing the compactness of the matrix structure while reducing shrinkage caused by structural loosening of the MKPC matrix. Between 800~1100°C, the shrinkage-inhibiting effect of MKPC mixtures diminishes following heat treatment, though some volume reduction persists. Notably, the 2.0% BF mixture exhibited a shrinkage rate at 1100°C that remained over 28% lower than the blank sample. This occurs because, although BF undergoes slight softening at high temperatures, its residual structure continues to provide structural support to the matrix, partially counteracting the shrinkage effects during sintering.

As shown in Figure 5c, when both AH and BF were added to the MKPC mixture, the shrinkage rates of most groups were significantly lower than the control group, and in many cases outperformed the modified groups with single components. Specifically, below 400°C, formulations with low AH content and high BF content (e.g., AH0.5-BF2.0) exhibited the most pronounced shrinkage inhibition, reducing the volume change rate by over half compared to the blank sample. Within the 600~800°C range, the mixture's volumetric shrinkage rate decreased further relative to the blank group, exhibiting nearly 60% lower shrinkage at 800°C compared to the control group. At 1000~1100°C, the mixture still outperformed the control group. Overall, formulations with higher BF content demonstrated more pronounced reductions in volumetric shrinkage both before and after heat treatment.

Based on the results of the above macro-performance tests, we selected AH15, BF1.0, and AH15-BF1.0 for microstructural analysis, the specific reasons are as follows: In the AH modified group, the AH15 group demonstrated the best strength retention and minimal mass loss after heat treatment. In Groups of, the BF1.0 group exhibited superior volume shrinkage suppression. In the BF modified group, the AH15-BF1.0 group achieved the highest room-temperature strength across all formulations.

3.5 XRD

The XRD patterns of four representative mixtures after heat treatment at room temperature, 400°C, 800°C, and 1100°C are shown in Figure 6. At room temperature, all mixtures exhibited intense diffraction peaks characteristic of hydrated potassium magnesium phosphate ($KMgPO_4 \cdot 6H_2O$). This compound constitutes the primary hydration product of MKPC and serves as the principal source of structural strength in

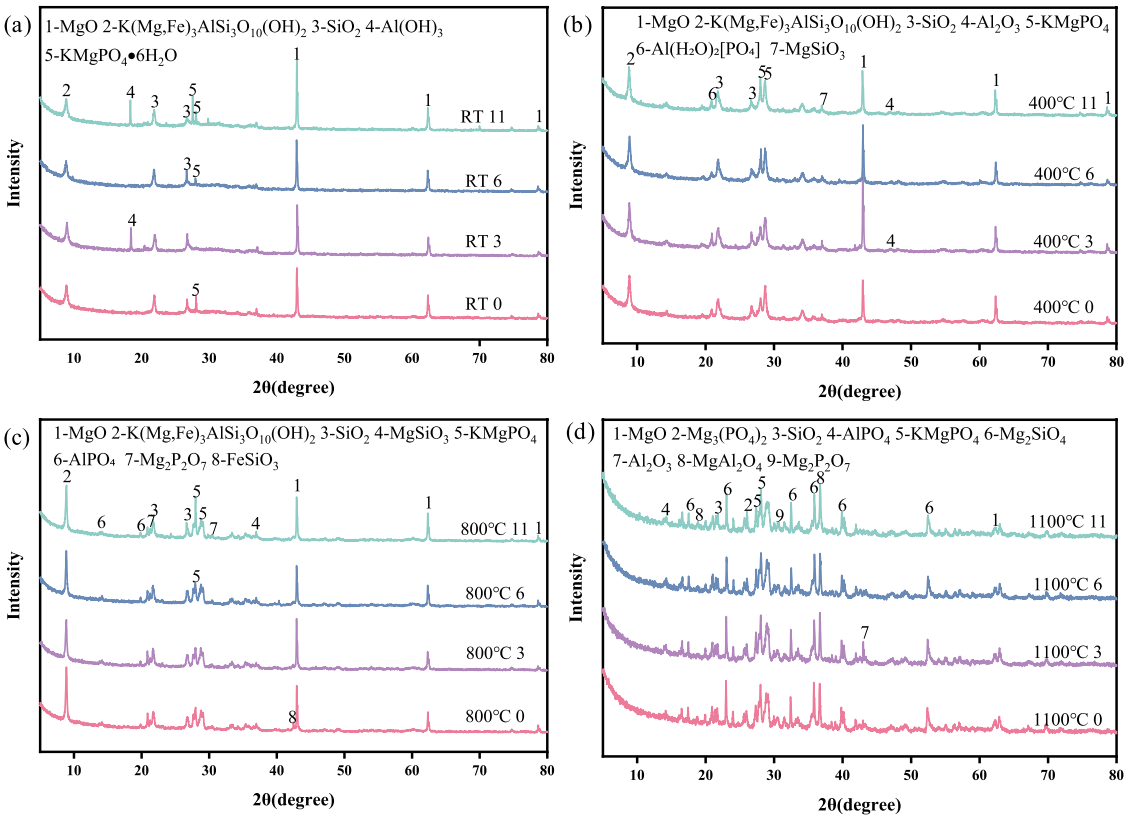

Figure 6 XRD pattern results of MKPC composites after heat treatment (a) room-temperature, (b) 400°C, (c) 800°C, (d) 1100°C, (group 0: blank, group 3: AH15, group 6: BF1.0, group 11: AH15-BF1.0)

the material. Additionally, residual MgO peaks, layered Mg-Fe aluminosilicate diffraction peaks from expanded vermiculite, and SiO_2 diffraction peaks from hollow glass microspheres are observable [1]. Distinct $Al(OH)_3$ diffraction peaks are discernible in Group 3 (AH15) and Group 11 (AH15-BF1.0).

After heat treatment at 400°C, the characteristic peaks of $KMgPO_4{\cdot}6H_2O$ were markedly diminished, whilst the reflection peaks corresponding to anhydrous potassium magnesium phosphate ($KMgPO_4$) became clearly discernible. Concurrently, in Groups 3 and 11, the peak intensity of $Al(OH)_3$ diminished and was replaced by reflections associated with Al_2O_3. This aligns with the thermal decomposition of aluminium hydroxide and the formation of rigid aluminium oxide. At this stage, faint reflections indicative of an aluminium-phosphate intermediate state were detectable in the AH-containing systems, suggesting the commencement of aluminium source reaction with phosphates during heating. Additionally, minor diffraction peaks for $MgSiO_3$ were observed, indicating initiation of the initial reaction between MgO and free SiO_2, though no other significant signs of reaction were apparent in the overall phase composition.

After heat treatment at 800°C, the phosphate within the MKPC mixture underwent further condensation and restructuring reactions, yielding distinct characteristic diffraction peaks for pyrophosphate ($Mg_2P_2O_7$), while the diffraction peak intensity of $KMgPO_4$ continued to diminish [39]. In mixtures containing AH, the diffraction peak of $AlPO_4$ markedly intensified, indicating that AH addition promoted the formation of the refractory aluminium phosphate phase. Concurrently, the $MgSiO_3$ peak became more pronounced, reflecting the ongoing silicate reaction. Furthermore, characteristic reflection peaks associated with the layered phase of vermiculite significantly diminished, suggesting that at this temperature, the layered structure of vermiculite gradually decomposed and underwent phase transformation at high temperatures.

After heat treatment at 1100°C, the MKPC mixture exhibited a marked phase transformation. Firstly, the diffraction peaks of $MgSiO_3$ and MgO disappeared, while the SiO_2 peak weakened markedly. Concurrently, a pronounced diffraction peak for magnesium olivine (Mg_2SiO_4) emerged. This indicates that between 1000~1100°C, residual magnesium and silicon phases within the system reacted to form a silicate-based refractory framework. Additionally, in mixtures containing AH, pronounced $MgAl_2O_4$ diffraction peaks and α-Al_2O_3 diffraction peaks emerge. This indicates that AH promotes the formation of high-melting-point, aluminium-bearing refractory phases within the system under high temperatures. Moreover, high-temperature phosphate phases (e.g., $Mg_3(PO_4)_2$) and residual $Mg_2P_2O_7$ remain detectable, whilst the original $KMgPO_4$ phase is markedly diminished. This aligns with the advanced transformation of K-Mg phosphate species under extreme thermal conditions.

Overall, the XRD results show that the MKPC system gradually evolved from hydrated phosphate phases at room temperature to more thermally stable phosphate, silicate and aluminate phases at elevated temperatures. Additionally,the clearer and sharper crystalline reflections observed in the AH-containing groups at high temperatures suggest a stronger ceramicisation tendency, which contributed to the improved high-temperature stability of the matrix.

3.6 SEM

Figure 7 presents the photographs of representative specimens (Blank, AH15, BF1.0, and AH15-BF1.0) after heat treatment at 400, 800, and 1100°C. It can be observed that the macroscopic appearance of all specimens changed progressively with increasing temperature, as reflected by colour variation, surface roughening, and the development of visible cracks. The Blank group showed relatively more pronounced cracking and integrity loss after high-temperature exposure, indicating severe thermal damage. In comparison, the AH15 specimens generally retained a more complete shape and denser surface morphology, suggesting that aluminium hydroxide contributed to improving the structural stability of MKPC during heating. The BF1.0 group exhibited comparatively better shape retention, which is consistent with the shrinkage-inhibiting effect of basalt fibres, although surface cracking was still visible at elevated temperatures. For the AH15-BF1.0 group, the combined addition of AH and BF helped maintain the overall specimen integrity to some extent, but thermal damage and crack development were still observed after exposure to higher temperatures.

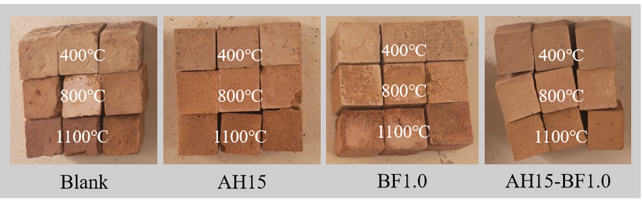

Figure 7 Photographs of the specimens after the high-temperature treatment

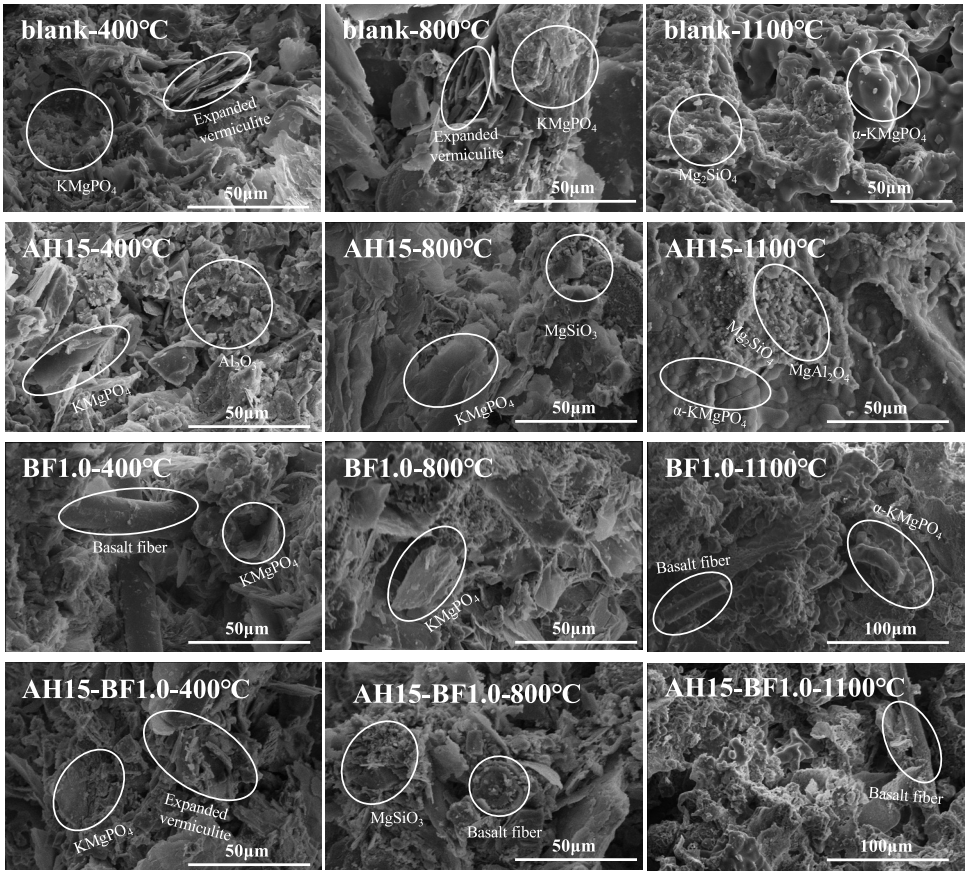

Figure 8 SEM images of MKPC cement after heat treatment

Figure 8 shows the microstructural morphology of samples from different groups after heat treatment. Results indicate that the microstructure of the MKPC sample in the control group deteriorated significantly following heat treatment. At 400°C, the matrix primarily comprised dehydrated phosphate phases exhibiting a loose, flocculent structure. Pores, microcracks, and the layered structure of expanded vermiculite were observable, indicating that the loss of bound water disrupted the continuity of the hydration product framework, though the expanded vermiculite provided some protective effect. At 800°C, the surface structure of the specimens was further compromised, exhibiting numerous fragmented particles alongside increased porosity and additional interfacial defects. Upon reaching 1100°C, pronounced phase restructuring and localised ceramicisation phenomena became observable. Based on XRD results, this is attributed to the formation of locally dense particle domains where high-temperature phosphates interact with refractory silicate phases (α-$KMgPO_4$, Mg_2SiO_4). Nevertheless, substantial residual porosity and structural damage induced by thermal stress remain observable throughout the system [40–42].

The microstructural characteristics of the MKPC samples doped with AH differed from those of the control group. After heat treatment at 400°C, numerous finely dispersed particles appeared on the sample surface, consistent with the dehydration decomposition products of $Al(OH)_3$. These particles partially filled and stabilised micro-pores, thereby mitigating damage to the MKPC matrix under high temperatures. At 800°C, intergranular bonding and sintering neck phenomena became more pronounced, with characteristic defect sizes markedly reduced. Concurrently, denser structural regions associated with Mg-Si reactions became observable, indicating that aluminium hydroxide addition lowered the temperature of partial phase reactions, accelerating phase transformations and thereby generating more stable phases. At 1100°C, the sample surface exhibited more pronounced ceramic-like structures characterised by particle aggregates connected via sintering necks and dense regions consistent with refractory phases. This demonstrates that adding aluminium hydroxide promotes the formation of a high-temperature resistant framework and suppresses structural collapse at high temperatures.

For the BF1.0 group, after heat treatment at 400°C, distinct fibre bridging phenomena were observable on the surface. Specifically, fibres penetrated the matrix structure, serving to bridge cracks while simultaneously forming spatial constraints that maintained the volumetric stability of the microstructure. As temperatures rose to 800~1100°C interfacial defects between fibres and the MKPC matrix increased, with localised

debonding occurring. This indicates that basalt fibres may undergo partial decomposition at high temperatures, diminishing interfacial load transfer capacity. Nevertheless, the three-dimensional fibre network continues to inhibit crack propagation through geometric confinement and effectively controls volumetric shrinkage. For the AH15-BF1.0 group, after heat treatment at 400°C, revealed basalt fibres and fillers co-embedded within the matrix. Following 800~1100°C treatment, although fibres visibly constrained the network structure to block crack propagation pathways, defects introduced by basalt fibres persisted. Overall, AH primarily enhances intergranular bonding by promoting the formation and sintering of refractory phases, while BF mainly suppresses deformation localisation through network support and crack bridging. These mechanisms complement each other, collectively improving structural integrity and enhancing resistance to high-temperature degradation.

In summary, AH primarily enhances intergranular bonding by promoting the formation and sintering of refractory phases, while BF primarily suppresses volumetric deformation through network support and crack bridging.

3.7 EDS

Figure 9 shows the EDS point-scan results acquired from the fractured cross-section of the AH15 sample after heat treatment at 1100°C. As observed from the micrograph, three representative morphological features can be distinguished: (i) relatively smooth and continuous matrix regions (point 3 and point 4), (ii) agglomerated zones consisting of abundant fine particulates attached to portions of the continuous phase (point 1 and point 2), and (iii) the marginal area at the boundary of the continuous phase (point 5).

The elemental distributions indicate that point 3 and point 4 are characterized by relatively high contents of K, P, O, and Mg, accompanied by low Si

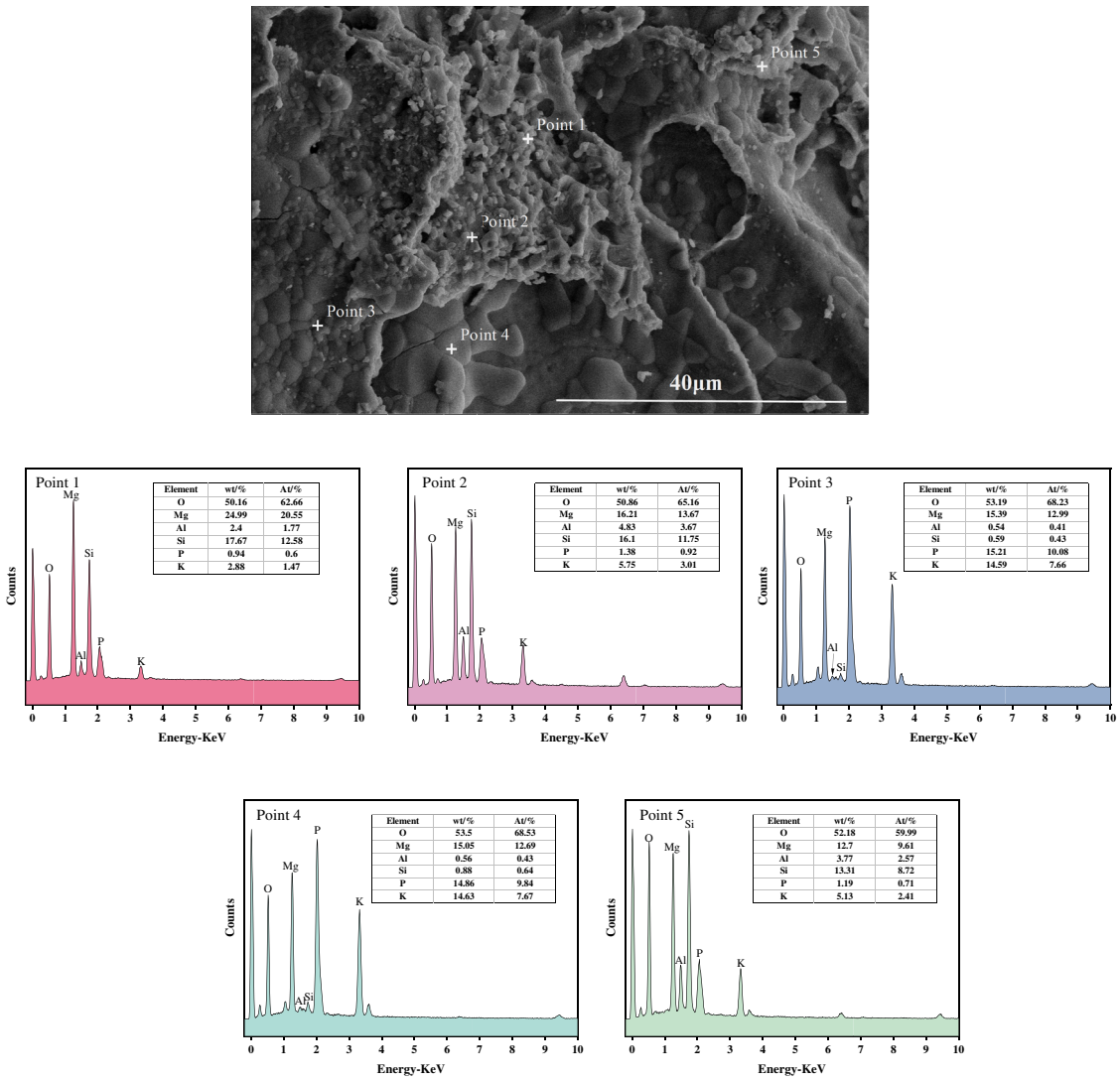

Figure 9 EDS scan images and spot elemental distribution results of AH15 samples after heat treatment at 1100°C

and Al contents, suggesting that these regions are dominated by K-Mg phosphate high-temperature phases. In conjunction with the XRD results in Figure 6d, the smooth, continuous region can be primarily attributed to phosphate-derived ceramic phases that transform at high temperatures, such as α-$KMgPO_4$ and $Mg_3(PO_4)_2$. These phases constitute the principal matrix components of MKPC after heat treatment at 1100°C.

In contrast, Points 1, 2, and 5 exhibit markedly lower K and P contents but significantly increased Si and Al contents. Based on the phase identification from Figure 6d, these regions are primarily associated with Mg_2SiO_4, α-Al_2O_3, SiO_2, and $MgAl_2O_4$. Notably, Point 1 and Point 2 show comparatively higher Mg and Si contents, whereas Point 5 is enriched in O. This compositional divergence implies that the fine-particle agglomeration zones contain higher fractions of forsterite (Mg_2SiO_4) and magnesium aluminate spinel ($MgAl_2O_4$), while the continuous-phase edge region (Point 5) is relatively enriched in α-Al_2O_3 and SiO_2.

Overall, from a macroscopic performance perspective, incorporating aluminium hydroxide (AH) can, within an appropriate dosage range, simultaneously enhance the room-temperature strength of MKPC and its high-temperature residual strength stability, while also providing a certain degree of shrinkage mitigation at intermediate-to-high temperatures. In contrast, basalt fibre (BF) proves more effective at improving high-temperature volumetric stability, but frequently results in reduced residual compressive strength and exhibits poorer strength stability under high-temperature conditions [6].

3.8 Mechanism analysis

Combining the test results of XRD, SEM and EDS, the mechanism of intensity changes in the control group at different temperatures is shown in Figure 10. At room temperature, $KMgPO_4 \cdot 6H_2O$ is the main cementitious phase, which provides the basic strength of the matrix. At 400°C, $KMgPO_4 \cdot 6H_2O$ dehydrates and decomposes into anhydrous $KMgPO_4$, meanwhile, the microstructure of MKPC specimens becomes loose due to water loss with increased pores and cracks, resulting in a decrease in strength. At 800°C, part of the anhydrous $KMgPO_4$ is further transformed into magnesium pyrophosphate ($Mg_2P_2O_7$), meanwhile, the layered structure of expanded vermiculite decomposes, the structural damage of the specimens is aggravated, and the strength drops to the lowest level. When the temperature rises to 1000°C and 1100°C, the active components released by the decomposition of expanded vermiculite react with SiO_2 from hollow glass microspheres and elements such as Mg and K in MKPC, forming a small amount of forsterite (Mg_2SiO_4) as a refractory phase, which leads to an improvement in the strength of the specimens after heat treatment at 1000°C and 1100°C compared with that at 800°C.

The mechanisms of action for AH and BF may be summarised as follows: For aluminium hydroxide, at ambient temperature, it primarily enhances matrix compactness through microfilling and interfacial regulation, whilst refining the scale of characteristic defects. This establishes a more continuous framework for subsequent thermal treatment. During heating, the dehydration reaction of AH not only absorbs substantial heat but also generates rigid Al_2O_3 particles that contribute to

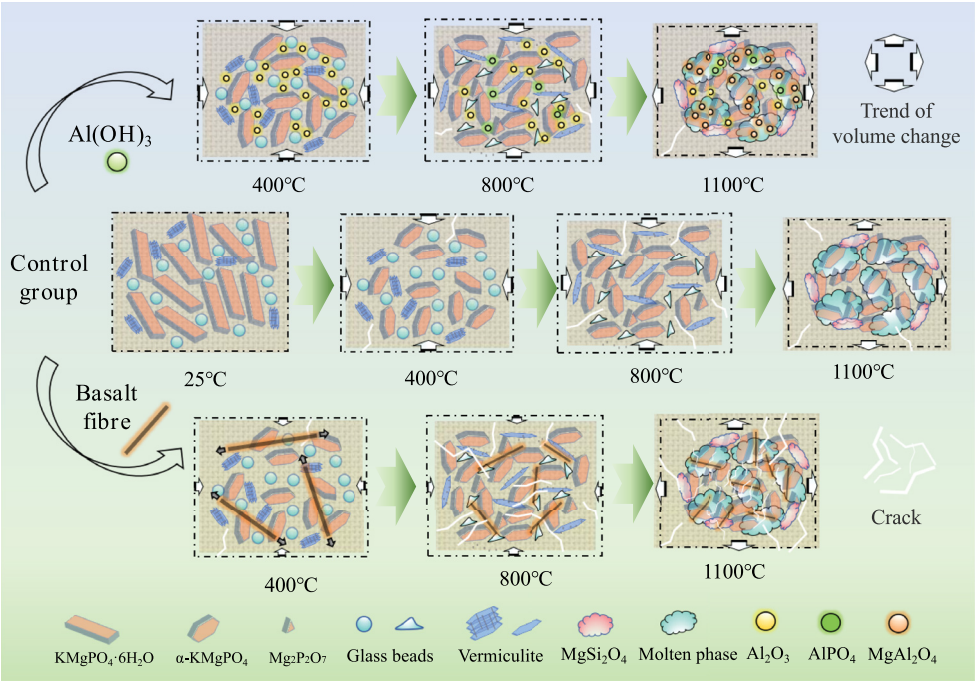

Figure 10 The influence mechanism of AH and BF on MKPC under different heat treatment temperatures

constructing a high-temperature resistant framework [43]. Concurrently, aluminium hydroxide also promotes the formation of refractory phases (e.g., $MgAl_2O_4$) and silicate ceramic networks. Furthermore, the newly formed refractory phases interact with phosphate phases to facilitate more continuous intergranular bonding, thereby enhancing load transfer efficiency and significantly mitigating strength loss caused by the dehydration and decomposition of hydration products.

With regard to basalt fibres, their primary function is based on the three-dimensional fibre network formed within the MKPC. Through continuous geometric confinement and crack bridging effects, they partially restrict thermally induced shrinkage and inhibit crack coalescence, thereby enhancing the volume stability of MKPC at high temperatures. However, under high temperatures, phase transitions within the basalt fibres themselves, coupled with thermal stresses within the system, readily induce delamination at the fibre-matrix interface and an increase in interfacial porosity. Under thermal stress, this reduces the effective load-transfer area and creates stress concentration points [20, 26]. Following thermal treatment, these regions may evolve into defect aggregation zones and preferential pathways for accelerated crack propagation, resulting in reduced residual compressive strength and deteriorated strength stability. Fundamentally, BF exhibits advantages in constraining deformation and inhibiting crack propagation. However, due to interfacial degradation and aggregate induction occurring after thermal treatment, MKPC mixtures incorporating BF exhibit severe strength degradation at high temperatures.

4 Conclusion

This paper systematically investigates the effects of aluminium hydroxide (AH) and basalt fibre (BF) as modifiers on the room-temperature and high-temperature performance of MKPC composites. The mechanisms of action were analysed through testing methods including XRD, SEM, and EDS. The main conclusions are as follows:

(1) At room temperature, both aluminium hydroxide (AH) and basalt fibre (BF) improved the compressive strength of MKPC composites containing expanded vermiculite and hollow glass microspheres. Compared with the control group (2.06 MPa), the compressive strength increased to 2.99 MPa for AH20 and to 3.53 MPa for BF2.0.
(2) AH shortened the setting process: both initial and final setting time decreased monotonically with increasing AH dosage. BF showed a non-monotonic effect on setting time, first decreased, then increased with fibre content, due to the competition between interfacial nucleation and fibre dispersion–agglomeration.
(3) After high-temperature exposure, AH effectively improved residual compressive strength. The AH15 mixture achieved the highest strength retention, with residual strengths 48.87%–101.59% higher than the control over the investigated temperature range, due to the *in-situ* formation of α-Al_2O_3 and $MgAl_2O_4$ refractory phases and strengthened ceramic bonding at high temperatures.
(4) BF markedly improved volumetric stability by restraining thermal shrinkage and bridging cracks, but reduced residual compressive strength at intermediate-to-high temperatures, and the deterioration became more severe as fibre dosage increased, due to fibre–matrix interfacial degradation and fibre strength degradation under thermal exposure, which weakened structural strength.

Based on the comprehensive evaluation of compressive strength, mass loss rate and volume shrinkage rate before and after high-temperature treatment, AH15 is recommended as the optimal mix proportion in this study, which presents the best balance between mechanical properties and high-temperature stability.

Acknowledgement

The authors would like to thank the State Key Laboratory of Silicate Materials for Architectures for providing technical support for the experimental testing.

Funding Statement

The financial support from Science and Technology Project of State Grid Zhejiang Electric Power Co., Ltd. (5211DS250005).

Author Contributions

Yutong Zhou: conceptualization, methodology, software, formal analysis, investigation, data curation, and writing—original draft. Zheng Zhou: conceptualization, validation, resources, supervision, writing—review and editing, funding acquisition, and project administration. Lvchao Qiu: resources and investigation. Zhoufeng Zhao: validation and supervision. Kuangda Lu: methodology. Liting Wang: investigation. Bo Peng: supervision. Shouwei Jian: methodology and software. Hongbo Tan: methodology. All authors reviewed and approved the final version of the manuscript.

Availability of Data and Materials

The data that support the findings of this study are available from the corresponding author upon reasonable request.

Ethics Approval

Not applicable.

Conflicts of Interest

The authors declare no conflicts of interest.

REFERENCES

[1] Fang C, Wen J, Li Y, Liu L, Shi Y, Lyu Y, et al. Effects of the modified expanded perlite materials on magnesium phosphate cement-based fireproof mortars: mechanical property, thermal conductivity and microstructure. Case Stud Constr Mater. 2025;22(2):e04140. doi:10.1016/j.cscm.2024.e04140.

[2] Fang B, Hu Z, Shi T, Liu Y, Wang X, Yang D, et al. Research progress on the properties and applications of magnesium phosphate cement. Ceram Int. 2023;49(3):4001–16. doi:10.1016/j.ceramint.2022.11.078.

[3] Chen SN, Lin C, Hsu HL, Chen XH, Huang YC, Hsieh TH, et al. Inorganic flame-retardant coatings based on magnesium potassium phosphate hydrate. Materials. 2022;15(15):5317. doi:10.3390/ma15155317.

[4] Zhuang J, Ni P, Xu R, Wu M. Dynamic properties of steel fiber-reinforced potassium magnesium phosphate cement-based materials after high-temperature treatment. J Clean Prod. 2023;429(2):139530. doi:10.1016/j.jclepro.2023.139530.

[5] Wang D, Yue Y, Mi T, Yang S, McCague C, Qian J, et al. Effect of magnesia-to-phosphate ratio on the passivation of mild steel in magnesium potassium phosphate cement. Corros Sci. 2020;174:108848. doi:10.1016/j.corsci.2020.108848.

[6] Koňáková D, Pommer V, Šádková K, Černý R, Vejmelková E. High-temperature resistance of cement composites with randomly distributed aluminium silicate fibers. Cem Concr Compos. 2024;145:105339. doi:10.1016/j.cemconcomp.2023.105339.

[7] Mei J, Dong C, He X, Li H, Chen H. Resistance of polymer modified calcium sulfoaluminate cement to sulphate attack. ZKG Int. 2023;3:54–61. doi:10.4028/www.scientific.net/amr.79-82.961.

[8] Wang X, Hu X, Yang J, Chong L, Shi C. Research progress on interfacial bonding between magnesium phosphate cement and steel: a review. Constr Build Mater. 2022;342(7):127925. doi:10.1016/j.conbuildmat.2022.127925.

[9] Dai X, Qian J, Qin J, Yue Y, Zhao Y, Jia X. Preparation and properties of magnesium phosphate cement-based fire retardant coating for steel. Materials. 2022;15(12):4134. doi:10.3390/ma15124134.

[10] Banerjee RH, Nelwamondo SMM, Raje N, Parab H, Chaudhary N, Mathi P, et al. Radiation stability testing of hydrated and heat-treated magnesium potassium phosphates for back end nuclear fuel cycle applications. Ceram Int. 2024;50(1):2405–14. doi:10.1016/j.ceramint.2023.11.023.

[11] Gao X, Zhang A, Li S, Sun B, Zhang L. The resistance to high temperature of magnesia phosphate cement paste containing wollastonite. Mater Struct. 2015;49(8):3423–34. doi:10.1617/s11527-015-0729-9.

[12] Qian W, Sun W, Guo S, Shi L, Yu G, Xian X. Effect of temperature variation on bonding properties of magnesium potassium phosphate cement: a multiscale analysis. Case Stud Constr Mater. 2024;21:e03993. doi:10.1016/j.cscm.2024.e03993.

[13] Li Y, Shi T, Chen B, Li Y. Performance of magnesium phosphate cement at elevated temperatures. Constr Build Mater. 2015;91:126–32. doi:10.1016/j.conbuildmat.2015.05.055.

[14] Fang Y, Yin X, Cui P, Wang X, Zhuang K, Ding Z, et al. Properties of magnesium potassium phosphate cement-expanded perlite composites applied as fire resistance coating. Constr Build Mater. 2021;293:123513. doi:10.1016/j.conbuildmat.2021.123513.

[15] Dai X, Ren W, Qin J, Jia X, Qian J. Influence and mechanism of borax on the physico-mechanical properties of magnesium potassium phosphate cement exposed to high temperatures. Constr Build Mater. 2023;376(2):131015. doi:10.2139/ssrn.4061567.

[16] Lin H, Guo Y, Zhi Z, Jiao Y, Wang L, Wang Y, et al. Study on mechanical strength and early hydration properties of cement paste modified by polycarboxylate superplasticizer with slump retention. ZKG Int. 2023;7:32–7.

[17] Mei J, Yuan C, Niu Y, Zhang J. Sulfate resistance of alkali-activated slag metakaolin fly ash cementitious materials. ZKG Int. 2024;1(1):50–9. doi:10.32604/zkg.2024.01.02.

[18] Liu Y, Chen Z, Ni H, Liu K, He J. High-temperature properties of fly ash and silica fume composite magnesium potassium phosphate cement. Constr Build Mater. 2024;441(6):137487. doi:10.1016/j.conbuildmat.2024.137487.

[19] Schwertmann T. Proposal for a new kiln process for burning of lump lime. ZKG Int. 2024;2(2):54–63. doi:10.32604/zkg.2024.02.03.

[20] Yasir M, Ahmad F, Megat-Yusoff PSM, Ullah S, Jimenez M. Quantifying the effects of basalt fibers on thermal degradation and fire performance of epoxy-based intumescent coating for fire protection of steel substrate. Prog Org Coat. 2019;132:148–58. doi:10.1016/j.porgcoat.2019.03.019.

[21] Yasir M, Amir N, Ahmad F, Ullah S, Jimenez M. Effect of basalt fibers dispersion on steel fire protection performance of epoxy-based intumescent coatings. Prog Org Coat. 2018;122:229–38. doi:10.1016/j.porgcoat.2018.05.029.

[22] Lou F, Wu K, Wang Q, Qian Z, Li S, Guo W. Improved flame-retardant and ceramifiable properties of EVA composites by combination of ammonium polyphosphate and aluminum hydroxide. Polymers. 2019;11(1):125. doi:10.3390/polym11010125.

[23] Chen SN, Li PK, Hsieh TH, Ho KS, Hong YM. Enhancements on flame resistance by inorganic silicate-based intumescent coating materials. Materials. 2021;14(21):6628. doi:10.3390/ma14216628.

[24] Li Y, Wang N, Long S, Wang Z, Lin H, Mu J. Research on the properties of brucite-based magnesium phosphate cement fire resistive coating for steel structures. Constr Build Mater. 2024;449:138481. doi:10.1016/j.conbuildmat.2024.138481.

[25] Tang D, Zhu L, Li X, Ren Y, Liu Y, Wang Q. Reinforced intumescent char combined with hollow glass microspheres to improve the fire-retardant and heat-insulation properties of fireproof coatings. Prog Org Coat. 2024;197:108839. doi:10.1016/j.porgcoat.2024.108839.

[26] Ding X, Zhang Y, Zhao Y, Bi J, Wang C, Shen M. Deterioration characteristics of basalt fiber-reinforced concrete under non-uniform cooling after high temperature exposure. Constr Build Mater. 2025;502:144366. doi:10.1016/j.conbuildmat.2025.144366.

[27] Qin J, Qian J, Li Z, You C, Dai X, Yue Y, et al. Mechanical properties of basalt fiber reinforced magnesium phosphate cement composites. Constr Build Mater. 2018;188(3):946–55. doi:10.1016/j.conbuildmat.2018.08.044.

[28] Jin Z, Wang L, Su Y, He X, Ma B, Wang Y, et al. Effect of different retarders on setting time and mechanical properties of hemihydrate phosphogypsum-calcium sulfoaluminate cement composite binder. Constr Build Mater. 2023;411(3):134339. doi:10.1016/j.conbuildmat.2023.134339.

[29] Li X, Chen X, Li X, Guo X, Yan Y, Li J, et al. Oyster-inspired, fast-drying, robust, and multifunctional waterborne uv-curable coating via phosphate chemistry strategy. ACS Sustain Chem Eng. 2025;13(21):7852–64. doi:10.1021/acssuschemeng.5c01019.

[30] Xue Y, Zhang S, Yang W. Influence of expanded vermiculite on fire protection of intumescent fireproof coatings for steel structures. J Coat Technol Res. 2014;12(2):357–64. doi:10.1007/s11998-014-9626-3.

[31] Yu B, Zhou J, Cheng B, Yang W. Compressive strength development and microstructure of magnesium phosphate cement concrete. Constr Build Mater. 2021;283(3):122585. doi:10.1016/j.conbuildmat.2021.122585.

[32] Le Rouzic M, Chaussadent T, Platret G, Stefan L. Mechanisms of k-struvite formation in magnesium phosphate cements. Cem Concr Res. 2017;91:117–22. doi:10.1016/j.cemconres.2016.11.008.

[33] Ding Z, Xu M-R, Dai J-G, Dong B-Q, Zhang M-J, Hong S-X, et al. Strengthening concrete using phosphate cement-based fiber-reinforced inorganic composites for improved fire resistance. Constr Build Mater. 2019;212:755–64. doi:10.1016/j.conbuildmat.2019.04.038.

[34] Zhang G, Wang Q, Li Y, Zhang M. Microstructure and micromechanical properties of magnesium phosphate cement. Cem Concr Res. 2023;172:107227. doi:10.1016/j.cemconres.2023.107227.

[35] Feng H, Lv L, Pang Y, Yuan C, Chu L, Zhao X. Bond behavior between the nano-Al_2O_3-water-glass-modified magnesium-phosphate-cement mortar and steel fiber. Constr Build Mater. 2021;306:124814. doi:10.1016/j.conbuildmat.2021.124814.

[36] Yazhenskikh E, Jantzen T, Hack K, Müller M. Critical thermodynamic evaluation of oxide systems relevant to fuel ashes and slags: potassium oxide–magnesium oxide–silica. Calphad. 2014;47:35–49. doi:10.1016/j.calphad.2014.05.006.

[37] Cau Dit Coumes C, Rousselet A, Xu B, Mercier CA, Gauffinet S. Investigation of aluminum nitrate as a set retarder of magnesium potassium phosphate cement: mechanisms involved in diluted suspension. Cem Concr Res. 2021;150:106608. doi:10.1016/j.cemconres.2021.106608.

[38] Tang D, Zhu L, Li X, Liu Y, Wang Q. Improved flame resistance and thermal insulation properties of steel fireproof coatings based on polyvinyl alcohol @ expandable graphite. Prog Org Coat. 2024;191:108444. doi:10.1016/j.porgcoat.2024.108444.

[39] Yan K, Yu X, Ren P, Zhang R, Oh E, Zhang Y, et al. Experimental research on fire resistance of the concrete beams strengthened with the CFRP sheets pasted by magnesium phosphate inorganic adhesive. Eng Struct. 2025;330:119946. doi:10.1016/j.engstruct.2025.119946.

[40] Zhai C, Li J, Xing J, An X, Zhang W, Yang R. A promising strategy for enhancing fire resistance of steel structure: a composite thermoplastic polyurethane sheet adhered to steel plate. Chem Eng J. 2024;488:150689. doi:10.1016/j.cej.2024.150689.

[41] Fang Y, Cui P, Ding Z, Zhu J-X. Properties of a magnesium phosphate cement-based fire-retardant coating containing glass fiber or glass fiber powder. Constr Build Mater. 2018;162(1):553–60. doi:10.1016/j.conbuildmat.2017.12.059.

[42] Ma X, Pan J, Cai J, Zhang Z, Han J. A review on cement-based materials used in steel structures as fireproof coating. Constr Build Mater. 2021;315(6):125627. doi:10.1016/j.conbuildmat.2021.125623.

[43] Li M, Pang L, Chen M, Xie J, Liu Q. Effects of aluminum hydroxide and layered double hydroxide on asphalt fire resistance. Materials. 2018;11(10):1939. doi:10.3390/ma11101939.